

# Multi-Mode Quantum Memories for High-Throughput Satellite Entanglement Distribution

Connor Casey,<sup>1,\*</sup> Albert Williams,<sup>2</sup> Catherine McCaffrey,<sup>1</sup> Eugene Rotherham,<sup>3</sup> and Nathan Darby<sup>4</sup>

<sup>1</sup>*Department of Physics, University of Massachusetts Amherst, Amherst, MA, USA*

<sup>2</sup>*College of Information and Computer Sciences,  
University of Massachusetts Amherst, Amherst, MA, USA*

<sup>3</sup>*Department of Space and Climate Physics, University College London,  
London, United Kingdom, London, United Kingdom*

<sup>4</sup>*Department of Physics, University of California, Santa Barbara, CA, USA*

(Dated: December 2, 2025)

Quantum networking seeks to enable global entanglement distribution through terrestrial and free-space channels; however, the exponential loss in these channels necessitates the need for quantum repeaters with efficient, long-lived quantum memories (QMs). Space-based architectures, particularly satellite-assisted links, offer a path to truly global connectivity; yet, they demand QMs that are compatible with orbital factors such as infrared radiation and the unique challenges of operating aboard a satellite. In this work, we propose a multimode quantum memory (MMQM) for Low-Earth Orbit (LEO) repeaters based on the atomic frequency comb (AFC) protocol. Our design integrates a hybrid alkali–noble-gas ensemble in an optical cavity, using alkali atoms for strong photon–matter coupling and noble-gas nuclear spins for minutes-to-hours coherence all without the need for cryogenics. The architecture natively supports temporal and spectral multiplexing, enabling the storage of 100 modes to parallelize probabilistic operations and overcome light-limited round-trip times. Representative link budgets at  $h = 500$  km with realistic apertures,  $\eta_{\text{mem}} \gtrsim 70\%$ , and  $t_{\text{buffer}}$  of several minutes predict improvements of up to two orders of magnitude in per-pass success probability and instantaneous SKR relative to a memoryless dual downlink, with clear scaling in  $N$ . Our contributions are: (i) a non-cryogenic, space-ready multimode memory; (ii) a systems analysis coupling mode count, storage time, and orbital geometry to achievable rate; and (iii) a near-term implementation roadmap. Together, these results indicate feasibility with current to near-term technology and provide a practical path toward a high-rate, space-enabled quantum internet.

## I. INTRODUCTION

Quantum networking aims to interconnect quantum computers, sensors, and communication systems by distributing quantum states and entanglement across geographically separated nodes [1]. While metropolitan-scale demonstrations have validated key primitives, extending such capabilities to continental and ultimately global distances remains challenging due to loss, noise, and the fundamental constraints of quantum mechanics [2, 3]. Unlike classical signals, quantum states cannot be amplified to compensate for attenuation due to the no-cloning theorem, which states that there is no unitary operation that can duplicate an arbitrary quantum state [4]. Consequently, error mitigation strategies such as quantum error correction and entanglement purification must be engineered to tolerate loss without violating the linearity of quantum mechanics [4, 5].

Terrestrial channels can illustrate what these concepts mean for practical applications. In optical fibers, transmission losses grow exponentially with distance, which limits practical direct links to a few hundred kilometers, even under favorable conditions [6, 7]. Free-space optical (FSO) links can mitigate exponential fiber loss by taking advantage of the inverse-square scaling of free-

space channels; however, turbulence, weather, and line-of-sight requirements are additional sources of error that collectively work to degrade performance in these channels [2, 8–10]. Satellite-based quantum communication leverages the near-vacuum environment of space and the favorable geometric scaling of free-space paths to enable intercontinental entanglement distribution, thus connecting isolated terrestrial clusters. [11–13]. In this hybrid architecture, satellites function as entanglement distribution hubs, feeding ground stations that, in turn, interface with optical fiber and local networks [13].

Even with satellite links, end-to-end performance at global scales ultimately relies on quantum repeaters [3, 14]. Repeaters divide a long path into shorter elementary links, generate entanglement locally, and extend it across the network via a method known as entanglement swapping [15]. For channels with high loss, techniques such as entanglement purification can ensure that the fidelity of the signal is maintained while creating end-to-end entanglement [16]. Because these steps are inherently probabilistic, a hardware component known as quantum memory (QM) acts as a buffer to store successful entangled pairs while other attempts proceed. This, in turn, avoids exponentially small coincidence probabilities and restores the polynomial scaling of the overall success rate [3]. Experimental implementations of these devices, therefore, require interfaces that can absorb and re-emit qubits on demand with high efficiency and fidelity

\* [cacasey@umass.edu](mailto:cacasey@umass.edu)

over application-appropriate storage times.

The requirements for space-based QMs are especially stringent when compared to their terrestrial counterparts. Many space scenarios demand adjustable delays from milliseconds to seconds—e.g., geostationary orbit to Earth ( $\sim 120$  ms (one way)) or Earth–Moon links ( $\sim 1.3$ s)—to synchronize heralding signals and enable feed-forward across long baselines [17]. Laboratory demonstrations have already achieved long-lived storage with high efficiency (e.g.,  $\eta > 70\%$  at  $\tau \sim 200$  ms), illustrating feasibility in principle [18]. By contrast, realizing comparable delays with fiber spools would incur prohibitive losses (e.g.,  $> 5,600$  dB for hundreds of milliseconds), underscoring the necessity of true quantum memories rather than passive delay lines [17]. Theory further indicates that space-deployed QMs can unlock truly global entanglement distribution by coordinating probabilistic operations over planetary distances [17, 19].

Multiple physical platforms are under active investigation for QMs, including ensemble-based media (e.g., cold and warm atomic gasses and rare-earth-ion-doped solids, REIDs) and single-emitter systems (e.g., NV centers, single atoms, and molecules). Optically active systems are particularly attractive because they natively interface with photonic qubits used for long-distance distribution. In repeater settings, these memories must support on-demand retrieval, high efficiency and fidelity, long coherence times commensurate with link latencies, and compatibility with entanglement swapping and purification. Cavity-enhanced atom–photon interactions (as in DLCZ-type schemes) provide one route to strong coupling for the generation and manipulation of stored excitations [20], while solid-state ensembles offer promising paths to integration and scalability.

Beyond these baseline requirements, multimode capacity emerges as a decisive lever for throughput. Modern networks achieve high data rates by exploiting parallelism; analogously, quantum networks benefit from memories that can store and process many independent photonic modes across temporal, spectral, or spatial degrees of freedom (or their combinations). As emphasized in prior work, “multimode capacity of [a] communication channel is an essential requirement for high data rates,” and a central challenge is realizing a quantum memory that simultaneously accommodates multiple single-photon modes [21]. The performance impact is immediate at the link level: if two single-mode memories are bridged by a channel of length  $L_0$  and refractive index  $n$ , the trial rate for heralded entanglement is bounded by the communication time  $\tau_{\text{comm}} = nL_0/c$ , yielding a maximum repetition rate  $R = 1/\tau_{\text{comm}}$  [22, 23]. For  $L_0 = 100$  km of fiber, this limits trials to  $R \approx 2$  kHz. A memory with  $N$  modes can parallelize attempts during each  $\tau_{\text{comm}}$ , boosting the heralding rate by  $\mathcal{O}(N)$  to first order [22, 23]. In large-scale networks—particularly those incorporating satellite segments where round-trip times are long—such parallelism is necessary to achieve high-throughput entanglement distribution that meets the de-

mands of practical applications.

In this work, we propose a multimode quantum memory (MMQM) protocol based on the atomic frequency comb (AFC) protocol tailored to Low-Earth Orbit (LEO) satellite networks. Our architecture uses a hybrid alkali–noble-gas ensemble inside an optical cavity, which combines the strong optical interface of alkali atoms with the long-lived coherence of noble-gas nuclear spins. This hybrid approach offers an intrinsically multimode interface with access to temporal and spectral multiplexing, while also enabling coherence times ranging from minutes to hours. Our objective is to specify a space-compatible MMQM architecture that aligns with the unique constraints of satellites and the operating environment aboard a satellite. By integrating multimode storage, future satellite-repeater constellations could utilize operations such as entanglement swapping and purification to help realize a truly global quantum internet.

## II. BACKGROUND

### A. Satellites, bosonic channels, and repeater motivation.

Free-space optical (FSO) satellite links are modeled as lossy bosonic channels with transmissivity  $\eta$  set by diffraction, pointing jitter, and atmospheric effects. In the absence of quantum repeaters, the private and quantum capacities of such channels obey repeaterless bounds that degrade strongly with loss [24, 25]. Quantum repeaters mitigate this by distributing entanglement over shorter elementary links and performing entanglement swapping, at the cost of requiring QMs, which preserve states through probabilistic heralding and classical signaling latency [26]. Critically, the required memory time scales inversely with the photonic transmission probability,  $T_{\text{mem}} \propto 1/P_{\text{trans}}$  [27]. Consequently, space-relevant memories should be (i) long-lived, (ii) optically interfaced for efficient photon–matter conversion, (iii) compatible with satellite constraints, and (iv) designed to function within the unique environment of space.

### B. Link geometries: uplink, downlink, and dual downlink.

In an uplink memory-assisted architecture, two ground stations send single photons (e.g., BB84-encoded) to a satellite that buffers them in distinct QMs; upon heralded loading of both memories, the satellite retrieves and interferes the photons in a Bell-state measurement (BSM) [28, 29]. Direct (QND) and indirect (entanglement-heralded) loading strategies have been analyzed [29]. The principal advantage of this approach is a high repetition rate; however, early-path atmospheric diffraction induces additional loss from the “shower curtain,” which is  $\sim 10$ – $20$  dB worse than downlink for comparable aper-

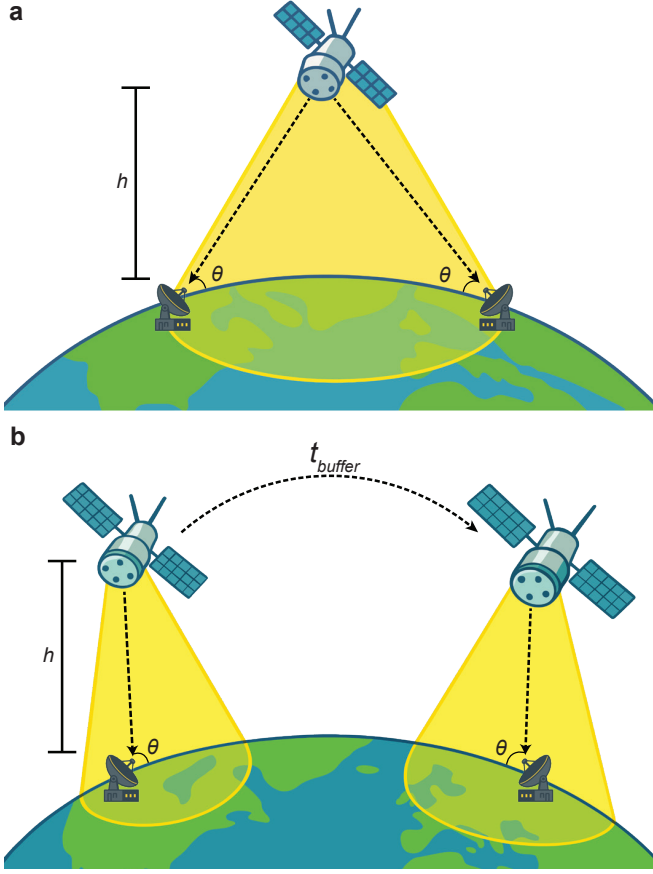


FIG. 1. **Buffered vs. dual downlink architectures.** (a) **Dual downlink:** An entangled-photon source transmits to two ground stations only during their co-view window. (b) **Buffered downlink (AFC-enabled):** One photon is downlinked while its partner is stored in an onboard AFC spin-wave memory; after a delay  $t_{\text{buffer}}$  (time between passes) the photon is recalled and sent to the second site, removing the simultaneous-visibility requirement. The memory must satisfy  $T_{\text{mem}} \geq t_{\text{buffer}}$  and contributes efficiency  $\eta_{\text{mem}}$  to the link budget. In both panels,  $h$  is satellite altitude,  $\theta$  the elevation angle; dashed lines are quantum channels and yellow cones are the satellite footprint.

tures. This shifts the burden to larger receivers in space and ultimately limits the range and key rate [30]. Representative budgets (e.g.,  $r_{\text{Tx}} = 15$  cm ground,  $r_{\text{Rx}} = 50$  cm space;  $\theta \sim 10$   $\mu\text{rad}$ ; 5 ms storage; 80% write-read; 20 MHz clock) show speedups over memoryless links to  $\sim 1450$  km but no straightforward path to multi-hop repeater nesting because photons propagate from ground  $\rightarrow$  space [30].

In a downlink variant, a central node emits photons entangled with each memory and transmits them to the ground stations. The central BSM then waits for classical heralds from the receivers, imposing a speed-of-light latency and hence second-scale storage times for  $\mathcal{O}(10^3)$  km baselines, unless parallelized via  $m$  memory pairs [30, 31].

Finally, dual-downlink entanglement distribution (E91) places the source onboard the satellite and sends one photon of each pair to each ground station. Because

the satellite does not need to be trusted, this approach aligns well with security goals and with modern (biased-basis) QKD post-processing [32–34]. In all cases, the physical link is a bosonic channel, so performance hinges on combating loss and background noise while maximizing spatial/temporal/spectral multiplexing to make up for the probabilistic nature of these approaches.

### C. Space-induced decoherence and satellite resource limits.

The environment of space differs dramatically from that of the laboratory. Natural ionizing radiation (cosmic rays, secondary particles) produces correlated errors and excess quasiparticles in solid-state devices, which degrades coherence and stability [35]. While photonic qubits are comparatively resilient, radiation and background light still load detectors and reduce state fidelity [36]. Ultra-high-fidelity operations must also contend with vacuum-fluctuation effects (e.g., Lamb-shift-scale level shifts) and tight thermal budgets given passive radiative cooling [37]. From a systems engineering perspective, power, mass/volume, and heat-lift are also scarce onboard a satellite, which constrains cryogenics, shielding, and onboard computing for real-time feed-forward/QEC [38]. Practical satellite nodes, therefore, favor compact, power-lean, and thermally tolerant memory platforms and detectors, such as space-qualified superconducting nanowire single-photon detectors (SNSPDs) [39]. Taken together, these environmental and resource constraints show that space-based hardware is more error prone and resource limited when juxtaposed with terrestrial laboratory systems.

### D. Ensemble based quantum memory candidates for space.

Ensemble based systems are especially attractive for space deployment because they interface directly with flying photons and entangled sources, support large optical bandwidths, and offer intrinsic multimode capacity in temporal, spectral, and spatial degrees of freedom [30]. Platforms currently under investigation include the following:

- **Warm vapors** (alkali) operate without laser cooling or cryogenics and already show noiseless and fast operation,  $\sim \text{GHz}$  bandwidth,  $\eta > 80\%$  with fidelity above the no cloning bound and  $\sim 1$  s storage in SERF like regimes; coupling to noble gas nuclear spins via spin exchange offers a path to hour scale coherence [40–43]. Compact vapor cell systems also have space heritage as optical frequency references on rockets and nanosats [44].
- **Laser cooled atomic ensembles** (including Bose Einstein condensates (BECs)) provide high optical

depth and low diffusion, enabling high efficiency, minute scale storage, and both temporal and spatial multiplexing [40, 41, 45–47]. Extensive micro-gravity and flight demonstrations together with experiments on the International Space Station attest to the growing attractiveness of this segment [48–59].

- **Rare earth ion doped crystals (REIDs)** at cryogenic temperatures combine narrow optical and spin transitions (long coherence) with strong multiplexing capability. Demonstrated performances include heralded intermemory entanglement, bright pulse storage from minutes to hours, and temporal, spectral, and spatial multimodality; integration via waveguides and nanophotonics improves compactness and light matter coupling [60–76]. Hybridized electron and nuclear spin levels in anisotropic hosts are particularly attractive for long lived, on demand storage while maintaining large optical bandwidths [76].

#### E. Atomic Frequency Comb (AFC) and multimode scaling.

AFC memories spectrally tailor an inhomogeneously broadened  $|g\rangle \leftrightarrow |e\rangle$  transition into a comb with tooth spacing  $\Delta$ . An incident photon excites a collective Dicke state that rephases after  $2\pi/\Delta$ , which yields an echo. A control pulse then maps this optical excitation to a spin state  $|s\rangle$  for on-demand retrieval and long-term storage. Backward retrieval can approach unit efficiency at high optical depth [77]. Importantly for repeaters, the AFC temporal multimode capacity is set by the number of teeth (i.e., the product of AFC bandwidth per channel, storage time, and the number of parallel channels) rather than by optical depth, as in EIT/Raman protocols [77]. Recent demonstrations at telecom wavelengths report the storage of  $\sim 10^3$ – $10^4$  modes (e.g., 1650 modes) with clear headroom via finer spectral packing and parallel spectral/spatial multiplexing [65, 66, 68, 78].

#### F. Implications for a satellite multimode memory architecture.

Coupling the bosonic-channel loss profile of FSO links and the inverse scaling of required memory time with transmission probability [27] to the practicalities of space operation [36–38], AFC-based multimode ensemble memories emerge as natural building blocks for space repeaters. They (i) raise the per-pass success probability via large temporal/spectral mode counts, (ii) leverage spin (including nuclear) degrees of freedom for long coherence times, and (iii) admit power-lean hardware components that are compatible with satellite constraints [30].

### III. PROTOCOL DESIGN

As seen in Figure 2, we consider an ensemble of  $N_a$  alkali-metal and  $N_b$  noble-gas atoms contained within a sealed glass cell mounted inside an optical cavity with one partially transmitting mirror, following the architecture of the original terrestrial design introduced in [79, 80]. Initially, the alkali spins are polarized along  $\hat{z}$  via optical pumping, while the noble-gas spins are polarized through spin-exchange optical pumping techniques.

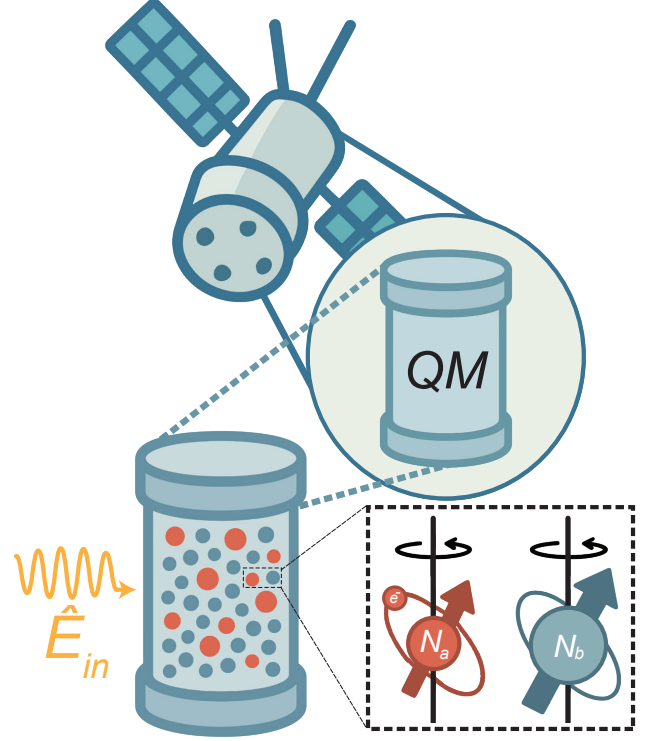


FIG. 2. **Satellite-borne hybrid alkali-noble-gas quantum memory.** An ensemble of  $N_a$  alkali-metal atoms (red) and  $N_b$  noble-gas atoms (blue) is contained in a sealed glass cell mounted inside a single-ended optical cavity with one partially transmitting mirror. Prior to operation, the alkali spins are polarized along  $\hat{z}$  by optical pumping and the noble-gas spins are polarized via spin-exchange optical pumping (SEOP). The incident optical mode  $\hat{E}_{in}$  drives the alkali transition  $|g\rangle \leftrightarrow |e\rangle$ ; the collective alkali spin  $\hat{S}$  couples to the noble-gas spin  $\hat{K}$  through spin exchange at rate  $J$ , mapping the excitation to the long-lived nuclear-spin mode and allowing re-emission as  $\hat{E}_{out}$ .

The alkali atoms are modeled as  $\Lambda$ -systems with a ground state  $|g\rangle$  and a metastable state  $|s\rangle$  coupled optically to the excited state  $|e\rangle$ , while noble-gas atoms are treated as two-level systems  $|\downarrow\rangle$  and  $|\uparrow\rangle$ . The quantum signal field  $\hat{E}$  couples  $|g\rangle$  to  $|e\rangle$ , and a classical control field with Rabi frequency  $\Omega$  couples  $|s\rangle$  to  $|e\rangle$ . A AFC is prepared on the inhomogeneously broadened  $|g\rangle \rightarrow |e\rangle$  transition using techniques such as piecewise adiabatic passage or optical frequency comb excitation, with peak



width  $\gamma$ , spacing  $\Delta$ , and total width  $\Gamma$ . The finesse is defined as  $F = \Delta/\gamma$ .

The cavity field obeys the Heisenberg–Langevin equation:

$$\partial_t \hat{E} = -\kappa \hat{E} + \sqrt{2\kappa} \hat{E}_{\text{in}} + i g_0^2 \wp \int_{-\infty}^{\infty} d\delta n(\delta) \hat{\sigma}_{ge}(t; \delta), \quad (1)$$

where  $\kappa$  is the cavity decay rate,  $g_0$  the atom–cavity coupling,  $\wp$  the dipole matrix element, and  $n(\delta)$  the atomic spectral distribution.

The atomic polarization evolves as:

$$\partial_t \hat{\sigma}_{ge} = -(i\delta + \gamma_p) \hat{\sigma}_{ge} + i\wp \hat{E}, \quad (2)$$

with  $\gamma_p$  the homogeneous linewidth. The input–output relation is:

$$\hat{E}_{\text{out}} - \hat{E}_{\text{in}} = \sqrt{2\kappa} \hat{E} \quad (3)$$

Defining collective spin operators for alkali and noble-gas ensembles:

$$\hat{S}(\mathbf{r}, t) = \frac{\hat{\sigma}_{gs}(\mathbf{r}, t)}{\sqrt{p_a n_a}}, \quad (4)$$

$$\hat{K}(\mathbf{r}, t) = \frac{\hat{\sigma}_{\downarrow\uparrow}(\mathbf{r}, t)}{\sqrt{p_b n_b}}, \quad (5)$$

the coupled evolution is:

$$\partial_t \hat{P} = -(\gamma_p + i\delta) \hat{P} + i\Omega \hat{S} + iG \hat{E} + \hat{f}_P, \quad (6a)$$

$$\partial_t \hat{S} = -(\gamma_s + i\delta_s - D_a \nabla^2) \hat{S} + i\Omega^* \hat{P} - iJ \hat{K} + \hat{f}_S, \quad (6b)$$

$$\partial_t \hat{K} = -(\gamma_k + i\delta_k - D_b \nabla^2) \hat{K} - iJ \hat{S} + \hat{f}_K \quad (6c)$$

Initially, with  $\Omega = 0$ , the quantum light is absorbed by the alkali ensemble. Perfect impedance matching ( $\kappa = Z$ ) ensures complete absorption:

$$\hat{E}_{\text{out}} = \frac{\kappa - Z}{\kappa + Z} \hat{E}_{\text{in}}, \quad Z = \frac{N_a g_0^2 \wp^2}{\Gamma} \quad (7)$$

The storage protocol proceeds in three main steps:

1. **Optical-to-alkali spin transfer.** Transfer the optical coherence to the alkali spin-wave  $\hat{S}$  using a chirped adiabatic pulse:

$$\langle \hat{S}^\dagger \hat{S} \rangle_T = \left[ 1 - \exp\left(-\frac{\pi T \Omega^2}{\Gamma}\right) \right] \langle \hat{P}^\dagger \hat{P} \rangle_0 \quad (8)$$

2. **Alkali-to-noble gas spin transfer.** Transfer  $\hat{S}$  to the noble-gas spin  $\hat{K}$  via spin-exchange collisions:

$$\langle \hat{K}^\dagger \hat{K} \rangle_{T'} = \exp\left(-\frac{\pi \gamma_s}{2J}\right) \langle \hat{S}^\dagger \hat{S} \rangle_T \quad (9)$$

3. **Long-term storage.** Store the excitation in  $\hat{K}$  for a duration limited by  $1/\gamma_k$ , which can potentially reach hundreds of hours.

Reversing the sequence after a delay leads to re-emission after  $2\pi/\Delta$ :

$$\hat{E}_{\text{out}}(t) = -\sqrt{\eta_m} \hat{E}_{\text{in}} \left( t - 2T' - 2T - \frac{2\pi}{\Delta} \right), \quad (10)$$

with efficiency:

$$\eta_m = \left[ 1 - \exp\left(-\frac{\pi^2 T \Omega^2}{\Gamma}\right) \right]^2 \exp\left(-\frac{\pi \gamma_s}{J}\right) \text{sinc}^2\left(\frac{\pi}{F}\right) \quad (11)$$

## A. Satellite-Specific Modifications

Deploying this memory in orbit requires proper consideration of the many spaceborne effects that would normally be absent in terrestrial deployments. First, the relative motion of a LEO satellite (with an orbital speed of several km/s) induces significant Doppler shifts in the optical frequencies, which are on the order of GHz for visible/near-IR wavelengths [82]. Without proper treatment, these Doppler offsets would detune the light from the alkali transitions and the cavity resonance. In practice, this is handled by real-time frequency tuning of the transmitter/receiver lasers based on the satellite’s ephemeris. Second, the free-space link coupling efficiency will be limited by diffraction and pointing errors. Even with diffraction-limited optics, a modest transmit aperture (e.g. 10–20 cm) yields a beam divergence on the order of 10.0  $\mu\text{rad}$ , so the spot size at the ground can be several meters across for typical LEO altitudes [30]. Coupling this free-space mode into the narrow mode of an optical cavity (or a single-mode fiber feeding the cavity) is lossy. Current designs of quantum transmitters estimate that only 50–60% of the collected light can be coupled into a single-mode channel, even under ideal alignment [83]. Any pointing and tracking jitter exacerbates this loss. For example, a  $\sim 2.0 \mu\text{rad}$  pointing error in a 20 cm downlink telescope can introduce an additional 4 dB loss in received power. The Micius quantum satellite demonstrated .60  $\mu\text{rad}$  pointing accuracy using two-axis gimballed telescopes and piezoelectric fast steering mirrors, which thus serve as the benchmark for our implementation [84]. Specifically, our system would employ a similar multi-stage acquisition and tracking approach: open-loop slewing to point the telescope within a fraction of a degree, followed by a beacon-based fine pointing loop and fast electro-optic beam steering to correct residual errors [84]. Lastly, atmospheric downlink effects must be considered. A downlink (satellite-to-ground) is generally preferred for quantum communication because the beam travels most of its path in the vacuum of free-space, with the dense atmosphere only being encountered at the end of the path. This avoids the dreaded “shower-curtain” effect of uplink channels, where turbulence near the transmitter greatly enlarges beam divergence early in the path [30]. Despite this, downlink channels still experience high

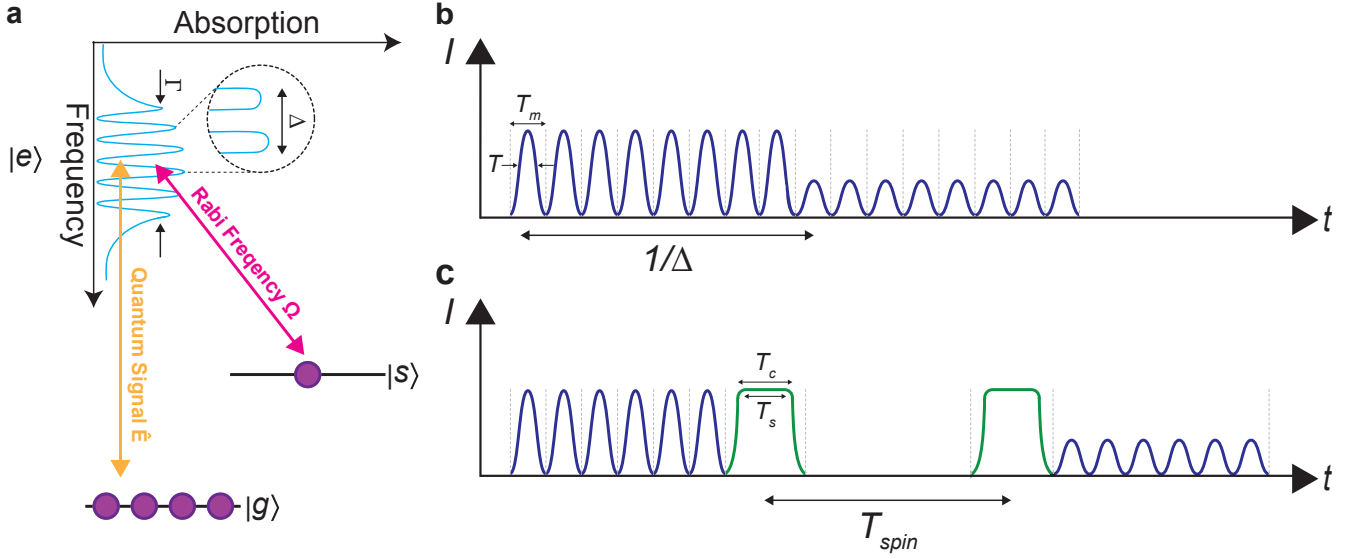


FIG. 3. **Atomic-frequency-comb (AFC) memory with fixed-delay and spin-wave readout.** (a) In an inhomogeneously broadened transition, frequency-selective pumping carves a periodic absorption comb of spacing  $\Delta$  and total bandwidth  $\Gamma$ . A weak quantum signal  $\hat{E}$  resonant with the comb is absorbed and re-emitted as an echo after the fixed rephasing time  $1/\Delta$  (two-level AFC). In the spin-wave variant, a control  $\pi$ -pulse coherently and reversibly transfers the excitation to a second ground state  $|s\rangle$ , enabling on-demand readout and long storage times. (b) Time sequence for the fixed-delay AFC: the input is a train of temporal modes of duration  $T_m$ , each mode containing pulses with intensity FWHM  $T$ ; the echo occurs at  $t = 1/\Delta$  (or as a train for multiple inputs). (c) Time sequence for the AFC spin-wave memory: a control pulse of duration (bin size)  $T_c$  interrupts the rephasing and stores the excitation as a spin wave for a programmable time  $T_{\text{spin}}$ . Because the control occupies part of the AFC window, the allowable input-mode window is reduced to  $1/\Delta - T_c$ ; a second control pulse reconverts the spin wave, yielding an on-demand echo at  $t = 1/\Delta + T_{\text{spin}}$ . Adapted from [81].

levels of atmospheric turbulence, which causes scintillation and wavefront distortions. Adaptive optics or feed-forward schemes may be used to partially correct the wavefront, but for a satellite transmitter with a small aperture, higher-order turbulence corrections yield only marginal gains [84].

#### 1. Microgravity Effects on Diffusion

The space-based cavity will operate in microgravity, which alters the gas dynamics within the memory cell. On Earth, any thermal gradients or concentration gradients in the vapor cell can induce convective currents that mix the gas. In microgravity, this buoyant convection is suppressed, and transport becomes purely diffusive [85]. The diffusion coefficients  $D_a$  (alkali vapor) and  $D_b$  (noble gas) themselves are functions of temperature and buffer gas pressure, and they are not fundamentally changed by gravity; however, the lack of convection means that these diffusion processes are the only means of distributing heat and mass in the cell. This has two main implications. First, without convective mixing, it may take longer for the alkali and noble-gas spin polarizations to reach a uniform steady state across the cell as spatial inhomogeneities must even out by diffusion alone. Second, any local heating (for instance, from the control laser or alkali pump light) will not be rapidly dissipated by fluid

motion. Thus, thermal gradients could persist longer and could create spatial variations in  $D_a$ ,  $D_b$  or in spin relaxation rates. The cell design must, therefore, minimize thermal hotspots, which could be achieved by using thermal straps, radiative cooling, and a small magnetic stirring field, all of which promote mixing [86, 87]. Overall, microgravity offers a more stable environment, which is beneficial for maintaining atomic coherence; however, it places the burden of careful thermal management to ensure that diffusion is sufficient to homogenize the spin ensemble behavior throughout the duration of the storage time.

#### B. Link Budget and Synchronization

For a satellite-based deployment, the quantum memory must interface with the free-space optical link while synchronizing with the satellite's visibility windows. The available contact time with a given ground station is limited to a few minutes per orbital pass (for LEO altitudes), so the protocol should efficiently multiplex and store as many photons as possible during each pass assuming line-of-sight is possible. The AFC-based multimode storage is well-suited for this: as illustrated in Fig. 4, the memory can absorb a train of temporal modes within the fixed cavity delay  $1/\Delta$ . In practice, one would operate the satellite as it comes into line-of-sight with a ground trans-

mitter by capturing successive entangled photon pulses into different temporal modes of the AFC. Immediately after absorption, these excitations are transferred to the long-lived nuclear spin ( $\hat{K}$ ) via the two-step process described earlier. This buffering in the noble-gas spin allows the satellite to fly out of view while the quantum states are safely stored in spin coherence. Once the satellite reaches another ground station (or comes around for a second pass over the same station, if coherence time allows), a retrieval sequence (spin-wave transfer back to alkali, then optical read-out) is initiated to re-emit the photons towards the receiver. Using realistic parameters – for example, a 15 cm diameter transmit telescope on the satellite and a 50 cm receive telescope on the ground, with  $10.0\ \mu\text{rad}$  beam divergence – one can expect on the order of  $10^{-4}$  end-to-end efficiency (around 40 dB loss) for a high-elevation pass [84, 88]. This assumes clear weather and high pointing accuracy. Under such conditions, if the source on the ground sends, say,  $10^6$  photons per second to the satellite, approximately 100 photons per second would enter the memory. Thanks to the multimodal capacity of the AFC (which can be in the range of  $N \sim 10^3$  modes, the satellite could accumulate a large batch of entangled photons in each overpass. [30]. The memory write/read efficiency and spin transfer efficiency then determine how many of those stored qubits can be retrieved with high fidelity. From this example, it is clear that high internal efficiency is essential for such a protocol to achieve high rates.

Therefore, our design targets near-unity as our goal for internal efficiency. To achieve this, we use impedance-matched absorption and optimal control pulses, as described by the theoretical efficiency  $\eta_m$  derived above. By synchronizing the storage protocol with the satellite’s pass through the use of GPS timing and closed-loop feedback from the ground for the control pulses, we ensure that the memory is ready to receive photons at the start of the pass and that all stored modes can be read out on demand at the appropriate time. This synchronization extends to Doppler shift management: the ground station’s transmitter can pre-compensate the frequency based on the known satellite velocity profile so that the incoming signal is always at the memory’s resonance [82]. In addition, both ground and satellite will share synchronized clocks to align the write/read timing within the photon coherence time [84]. Overall, these considerations ensure that the satellite memory can effectively integrate into a quantum network, capturing entanglement on the fly and releasing it when and where needed to perform entanglement swapping or to deliver a secret key.

### C. Space Payload Engineering Constraints

Implementing the above capabilities on a satellite needs to be achievable, despite the payload constraints of a LEO satellite. We draw on proven strategies from ultracold atom experiments in space—notably, NASA’s Cold

Atom Lab (CAL) aboard the International Space Station—to guide our design. CAL had to maintain an ultrahigh vacuum and stable conditions for Bose–Einstein condensates in orbit, which closely parallels the needs of our spaceborne quantum memory. In CAL’s design, a compact dual-chamber glass cell was used, with one science cell kept below  $10^{-10}$  Torr by a combination of a miniaturized ion pump and non-evaporable getter (NEG) pumps [89]. We similarly require a long-lived cell for the alkali–noble gas mixture; although our memory cell is sealed and does not need active pumping during operation, it must be processed to high vacuum standards to remove impurities and avoid excess alkali vapor pressure at operating temperature. A small getter pump can be included to absorb any outgassing over the mission lifetime. Surrounding the cell and cavity, magnetic shielding is essential. CAL employed a dual-layer metal magnetic shield to attenuate the strongly fluctuating magnetic fields on the ISS [89]. Our satellite will encounter Earth’s magnetic field, as well as the spacecraft-induced fields. We believe a similar dual-layer shield can reduce ambient field exposure, which will ensure the spin precession frequencies ( $\delta_s, \delta_k$ ) remain stable. Additional coil systems inside the shield can provide fine bias field control and enable rapid re-zeroing of fields if, for example, a magnetic disturbance from the satellite occurs. Vibration isolation and mechanical stability are also important factors to consider. Launch and deployment subject the payload to high vibration and shock. Even in orbit, reaction wheel jitter or thermal flexing could misalign the cavity. In CAL, all the delicate optics (mirrors, fiber collimators, cameras) were mounted on a solid aluminum support structure that was attached to the physics package [89]. This ensured that any mechanical drift affecting all components was addressed and that the relative alignments were kept fixed. We adopt the same approach in our design: the cavity mirrors, coupling lenses, and detector optics will be integrated onto a single optical bench bonded to the vacuum package. Passive vibration damping, such as gel mounts or commercial shock absorbers, will protect the system during launch, and once in microgravity, the lack of seismic noise greatly benefits cavity stability. For the optical cavity specifically, we will use low-expansion materials and possibly small piezoelectric actuators to lock its length to the atomic resonance, counteracting thermal or mechanical drift.

Radiation in orbit poses another challenge. High-energy cosmic rays and solar particles can induce radiation damage or create errors such as bit flips in control electronics, or even spin flips in the atoms due to ionization events [90]. CAL did not incorporate dedicated radiation shielding beyond the ISS hull; however, for our design, we must consider it. Specifically, our design uses radiation-hardened electronics (FPGA and microcontrollers rated for space) and places sensitive components (detectors, avalanche photodiodes, etc.) in lightweight shielding enclosures to block a significant portion of ionizing radiation [91]. The alkali/noble gas atoms

themselves are somewhat shielded by the vacuum cell walls and surrounding optics, but prolonged exposure to cosmic rays could lead to glass cell charging or diffusion of impurities. We will mitigate this by using a conductive coating on the cell to dissipate charges [92].

Thermal control is another crucial aspect that we must consider in our design. A satellite experiences rapid temperature swings as it moves in and out of sunlight. The hybrid memory, especially the vapor cell and cavity, must be kept within a narrow temperature range for optimal operation (typically, alkali vapor cells are heated to  $\sim 40\text{--}80^\circ\text{C}$  for sufficient vapor density, and the cavity must remain stable to much better than that to avoid drift in resonance). We implement a combination of passive and active thermal regulation. Externally, the payload is blanketed in multilayer insulation (MLI) to reduce radiative exchange with the environment, and heat is conducted to dedicated radiator panels that disperse waste heat to space. Internally, key components are thermally linked via high-conductivity straps (as in CAL’s water-cooled thermal straps for its coil assembly) to even out temperature gradients [89]. Small resistance heaters with closed-loop PID control are attached near the cell and cavity to fine-tune their temperatures. On the CAL ISS experiment, fluid loops were used for cooling; however, but for our satellite, we prefer heat pipes or pumped liquid loops only if absolutely necessary due to mass and power overhead [93]. Instead, our design relies mainly on passive thermal stability, using the thermal mass of the optical bench and a low conductivity mounting to the satellite chassis to decouple fast fluctuations. All told, these engineering measures build upon the CAL experiment and other space quantum hardware demonstrations to ensure the quantum memory operates as intended in space.

#### D. Implementation

Following the original implementation from [80, 94], we consider a mixed  $^3\text{He}\text{--K}$  ensemble confined in an uncoated spherical glass cell of radius  $R = 1\text{ cm}$  at  $215^\circ\text{C}$ . We operate in a high pressure configuration with working densities  $n_a = 5.0 \times 10^{14}\text{ cm}^{-3}$  for potassium and  $n_b = 6.0 \times 10^{19}\text{ cm}^{-3}$  for  $^3\text{He}$  [95]. The coherent spin exchange coupling used in the simulations is set to  $J = 2.00 \times 10^{-5}$  [79]. A nitrogen buffer gas at 30 Torr is included for collisional quenching, which broadens the K  $D_1$  transition to a linewidth of  $\Gamma \approx 27\text{ GHz}$ . The AFC tooth width  $\gamma$  is limited by the optical coherence lifetime and is bounded by twice the natural linewidth  $\gamma_p = 5.96 \times 2\pi\text{ MHz}$ . Targeting a finesse  $F = 8$  gives a tooth spacing  $\Delta = 96\text{ MHz}$  [79].

Assuming the AFC bandwidth matches the pressure broadened line, the multimode capacity is

$$M = \frac{2\Gamma}{5\Delta} = \frac{2 \times 27\text{ GHz}}{5 \times 96\text{ MHz}} = 112.$$

For our quantum memory simulation, we use coupled spin-diffusion dynamics with Dirichlet boundary conditions for the alkali component and Neumann for the noble gas. When operating the satellite abroad, we expect a slightly higher steady state gas temperature due to the requirements of a stable thermal management system aboard. Due to advancements in current thermal management systems, we see this being minimal, as seen in [54]. In addition to this, the pressure differential across the optical cavity seals and the outside environment increases in orbit relative to the ground. In turn, we expect a modest reduction in the fill pressure of the cavity. Because the diffusion of a dilute gas scales approximately as  $D \propto T^{3/2}/P$  according to Chapman Enskog theory [96], we increase the diffusion constants by 10% from the original paper, which gives  $D_a = 1.02 \times 10^{-8}\text{ m}^2/\text{s}$  and  $D_b = 2.05 \times 10^{-8}\text{ m}^2/\text{s}$  respectively. For small detunings, we set  $\delta_s = 0$  and  $\delta_k = 1.11 \times 10^{-3}$  [79]. For longitudinal relaxation rates, we set  $\gamma_k = 0$  and  $\gamma_s = 3.1 \times 10^{-7}\text{ s}^{-1}$  [79]. All values were derived from the original study, with some updated to reflect the fact that this memory will be operating in space.

Building a satellite-borne alkali-noble gas quantum memory will require the integration of the above considerations into a satellite-ready system where miniaturization and integration will be key. Fortunately, the core of the memory—a vapor cell and optical cavity—can be quite compact. For example, the entire dual-cell vacuum chamber used in CAL had dimensions on the order of a few centimeters, and compact vapor cells with integrated nano-coating technology have been demonstrated for atomic clocks and magnetometers [89, 97]. Utilizing recent developments in integrated photonics and micro-optics, the cavity could be formed by tiny high-reflectivity mirrors directly bonded to the cell or on a ceramic spacer, and semiconductor diode lasers (in the 780–800 nm range) can be made flight-qualified and small. The control and readout lasers might be fiber-coupled distributed Bragg reflector (DBR) lasers, locked via spectroscopy to an onboard reference cell. All laser beams can be delivered through polarization-maintaining fibers to the memory module, similar to the fiber-fed design of CAL’s optical system [89]. The entire science module, which contains the memory cell, cavity, minor optical elements, and shielding – would be mounted on a small optical bench ( $\sim 30\text{ cm}$ ) and could fit inside a microsatellite (50–100 kg class) or possibly even a 12U CubeSat with careful design. The electronics (RF coils for driving spin transitions, laser drivers, single-photon detectors, and a processor for control logic) would occupy another section of the satellite bus, which is designed with redundancy and fail-safes typical of space missions.



#### IV. SYSTEM MODEL

This section defines our space-to-ground (S-G) link model and how we quantified the success of our memory proposal. We factor the per-trial success probability into source, memory, detector, atmospheric, and diffraction/pointing terms, each with explicit elevation/slant-range dependence. We then compute SKR under BB84 with one-way post-processing and compare two geometries: (i) dual downlink at fixed low elevation, and (ii) buffered overhead with zenith links subject to  $T_{\text{mem}} \geq t_{\text{buffer}}$ .

##### A. Link Budget

We model each S-G elementary link as a product of statistically independent transmission factors. The single-shot success probability is

$$\eta_{\text{S-G}} = \eta_{\text{src}} \eta_{\text{mem}} \eta_{\text{det}} \eta_{\text{atm}}(\theta) \eta_{\text{dif}}(l), \quad (12)$$

where  $\eta_{\text{src}}$  is the entangled-photon source efficiency,  $\eta_{\text{mem}}$  the memory write/read efficiency on the satellite,  $\eta_{\text{det}}$  the (ground) detector efficiency,  $\eta_{\text{atm}}(\theta)$  the single-pass atmospheric transmission at elevation  $\theta$ , and  $\eta_{\text{dif}}(l)$  the diffraction + pointing coupling over slant range  $l$ . For the configurations studied here we use

$$\eta_{\text{src}} = 0.20, \quad \eta_{\text{mem}} = 0.74, \quad \eta_{\text{det}} = 0.70. \quad (13)$$

*a. Atmospheric transmission.* Single-pass attenuation along the slant path at elevation  $\theta$  follows a simple air-mass model:

$$\eta_{\text{atm}}(\theta) = (\eta_{\text{atm}}^z)^{1/\sin \theta}, \quad (14)$$

where  $\eta_{\text{atm}}^z$  is the zenith transmission (set by wavelength and site conditions).

*b. Diffraction and pointing.* Collected power at the ground telescope is expressed as

$$\eta_{\text{dif}}(l) = \frac{P(l)}{P_0}. \quad (15)$$

A diffraction-limited Gaussian beam of waist  $w_0$  obeys

$$\theta_d = \frac{\lambda}{\pi w_0}, \quad w(z) = w_0 \sqrt{1 + \left(\frac{\theta_d z}{w_0}\right)^2}, \quad (16)$$

$$I(r, z) = I_0 \left(\frac{w_0}{w(z)}\right)^2 \exp\left[-\frac{2r^2}{w(z)^2}\right]. \quad (17)$$

Residual pointing jitter is modeled by a 2D Gaussian kernel with rms  $\sigma_p$ :

$$g_p(\mathbf{r}) = \frac{1}{2\pi\sigma_p^2} \exp\left(-\frac{\|\mathbf{r}\|^2}{2\sigma_p^2}\right), \quad (18)$$

and the received intensity is the convolution  $\tilde{I} = I * g_p$ . Power coupled into a circular pupil of radius  $R_{\text{rec}}$  at range  $l$  is

$$P(l) = \int_0^{R_{\text{rec}}} \rho d\rho \int_0^{2\pi} d\varphi \tilde{I}(\rho, l). \quad (19)$$

*c. Geometry.* The elevation  $\theta$  and slant range  $l$  are determined from the ground-track separation  $L_g$  and orbital altitude  $h$ :

$$l^2 = R_E^2 + (R_E + h)^2 - 2R_E(R_E + h) \cos\left(\frac{L_g}{R_E}\right), \quad (20)$$

$$\theta = \frac{\pi}{2} - \frac{L_g}{R_E} - \arcsin\left[\frac{R_E}{l} \sin\left(\frac{L_g}{R_E}\right)\right], \quad (21)$$

with  $R_E = 6,371$  km. For a more detailed overview of the parameters used in this study, see Appendix B.

#### V. RESULTS & ANALYSIS

We first visualize the memory dynamics, then quantify SKR gains, and finally compare the two different operational scenarios.

##### A. Downlink Link Establishment Probability

Figure 5 maps the single-photon downlink success probability  $\eta$  as a function of slant range and rms pointing jitter. Two features dominate: (i) diffraction loss with increasing range and (ii) the strong penalty from microradian-level jitter, which broadens the far-field spot relative to the receive pupil. Operating near zenith (short range) substantially mitigates both effects.

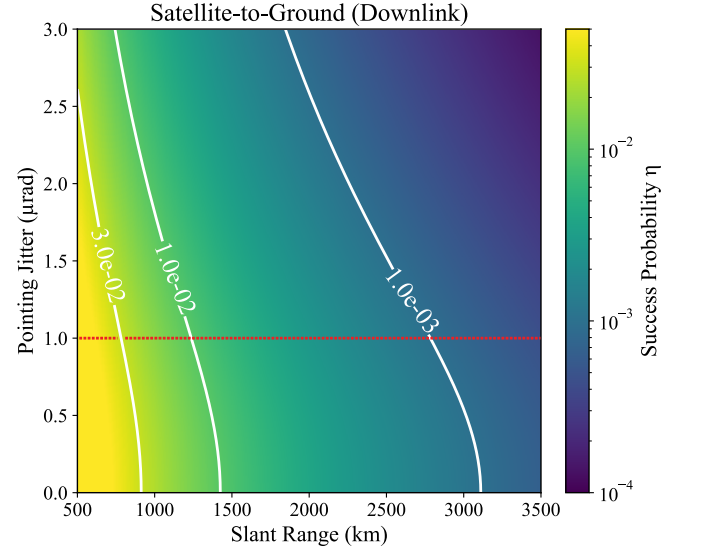


FIG. 5. **Satellite-to-ground downlink success probability.** Color indicates the single-photon success probability  $\eta$  as a function of slant range (horizontal axis) and rms pointing jitter (vertical axis); white curves are iso- $\eta$  contours. Larger range and/or jitter reduce  $\eta$  due to diffraction and pointing loss. The red dashed line marks the operating assumption for pointing-jitter used in this work (rms of 1.0  $\mu\text{rad}$ ).

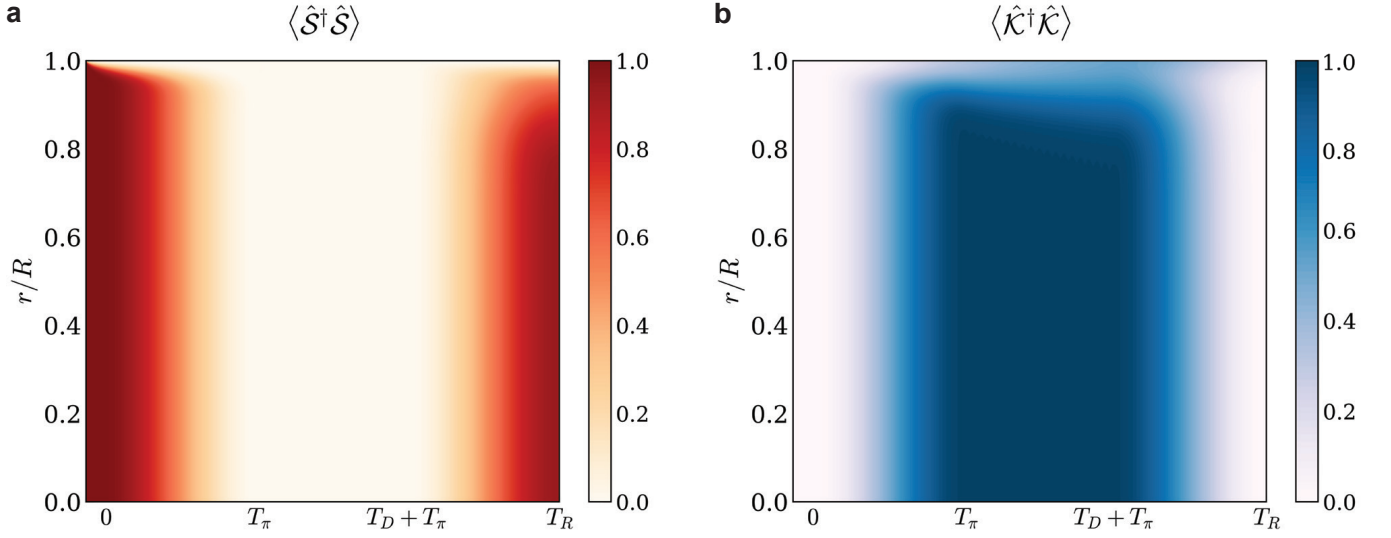


FIG. 4. **Spatiotemporal kymographs of the collective spins.** (a) Alkali-spin kymograph: color encodes the normalized magnitude  $\langle \hat{S}^\dagger \hat{S} \rangle(r, t)$  on a radial slice of the cell where  $r$  is the distance from the center and  $R$  is the cell radius. The normalized radial slice of the cell runs from  $r/R \in [0, 1]$  where 0 is the center and 1 is the wall which is shown over time. The bright bands at the write and read instants  $T_\pi$  and  $T_R$  indicate loading and retrieval of the alkali spin wave; attenuation during the dark interval  $T_D$  reflects homogeneous decay  $\gamma_s$  and diffusion  $D_a$ . (b) Noble-gas-spin kymograph: color encodes  $\langle \hat{K}^\dagger \hat{K} \rangle(r, t)$ . Population builds during the alkali  $\rightarrow$  noble-gas transfer at  $T_\pi$  via spin-exchange  $J$ , remains high throughout storage with mild edge losses from wall relaxation and diffusion  $D_b$ , and then maps back at  $T_R$ . Both panels are obtained by solving the coupled spin-diffusion equations (Eqs. (6a)–(6c)) and plotting the azimuthally averaged  $|S(r, t)|^2$  and  $|K(r, t)|^2$ , each normalized to the initial optical excitation.

### B. Memory Efficiency

Utilizing the code from [79], we compute the expectation values of the collective spins for the alkali and noble-gas ensembles over the full protocol by numerically integrating the coupled spin equations (Eqs. (6a)–(6c)). Spatial discretization uses the method of lines, and time integration employs a time-adaptive Runge–Kutta scheme. The boundary conditions for these equations follow the physical surface interactions of the two species. At the glass–vapor interface, the alkali polarization is set to zero (Dirichlet):

$$S(r = R, t) = 0.$$

This destructive boundary condition properly accounts for the fact that alkali atoms undergo strong depolarizing collisions with uncoated cell walls, which scramble the electronic spin and prevent coherent spin-wave amplitude from surviving at the boundary [98, 99]. As a result, alkali coherence decays toward the wall and is effectively quenched at  $r = R$ . Thus, from this, we see that the spatial spin-wave mode will be naturally localized toward the central region of the cell.

In contrast, the noble-gas nuclear spin exhibits extremely weak depolarization in collisions with clean glass walls, so that wall limited relaxation times approach hundreds of hours even in small cells [100]. To capture this, we impose a von Neumann boundary condition on the noble-gas spin, which therefore meets the following con-

dition:

$$\partial_r K(r, t)|_{r=R} = 0.$$

This corresponds to a non-destructive, reflective boundary where no polarization current flows through the wall. Physically, this enforces that the noble-gas polarization remains smooth across the boundary and that the wall does not act as a relaxation sink, which allows coherence to remain stable for hundreds of hours, as we observe in experiments.

### C. Instantaneous SKR (Space-to-Ground)

We quantify the instantaneous secret key rate (SKR) for a S-G entanglement distribution link using the standard asymptotic lower bound for BB84 with one-way post-processing. Per channel use, the secret key fraction is

$$R = \frac{Y}{2} [1 - h(e_X) - f h(e_Z)], \quad (22)$$

where  $Y$  is the success probability per channel use that the protocol is heralded (e.g., both parties register a valid detection and the Bell-state measurement succeeds),  $e_X$  and  $e_Z$  are the quantum bit error rates (QBERs) in the  $X$  and  $Z$  bases, and  $f \geq 1$  captures error-correction inefficiency. This expression follows Refs. [29–31]. The binary

entropy function is

$$h(e) = -e \log_2 e - (1-e) \log_2 (1-e). \quad (23)$$

Details of how  $Y$  and the individual error terms are computed for the link model are provided in Refs. [29, 101, 102].

Given a channel-use rate (e.g., pair-generation or pulse)  $\nu$  [s<sup>-1</sup>], the instantaneous SKR is

$$R_{\text{inst}}(t) = \nu(t) R(t), \quad (24)$$

which may vary over a pass through its time dependence in the elevation angle(s), losses, and background.

*a. Yield decomposition.* For the S-G geometry, we write

$$Y(t) = P_{\text{herald}} \eta_A(t) \eta_B(t), \quad (25)$$

where  $P_{\text{herald}}$  is the protocol-specific heralding probability (e.g., Bell-state measurement success), and  $\eta_A(t), \eta_B(t)$  are the end-to-end transmission efficiencies from the satellite to each optical ground station (OGS), including diffraction, atmosphere, pointing, receiver optics, detector efficiency, and (when used) memory efficiency. The elevation-angle dependence enters through the slant path  $L_s(\theta)$  and the corresponding atmospheric and geometric losses.

*b. Scenarios considered.* We evaluate two operational cases that differ only in pointing geometry and the use of buffering:

1. **Dual-downlink.** A single satellite distributes entangled photon pairs (EPS) simultaneously to two OGS, each tracked at a fixed low elevation, here  $\theta_A = \theta_B = 20^\circ$ . The longer slant ranges  $L_s(20^\circ)$  reduce  $\eta_{A,B}$ , so that

$$Y_{\text{dual}}(t) = P_{\text{herald}} \eta_A(\theta_A = 20^\circ, t) \times \eta_B(\theta_B = 20^\circ, t), \quad (26)$$

$$R_{\text{inst,dual}}(t) = \nu(t) \frac{Y_{\text{dual}}(t)}{2} [1 - h(e_X) - f h(e_Z)]. \quad (27)$$

2. **Buffered downlink.** A single satellite performs two *sequential* zenith downlinks. First, it transmits to OGS A at  $\theta = 90^\circ$ ; at zenith the slant range equals the orbital height,

$$L_s(90^\circ) = h. \quad (28)$$

The detected (or heralded) qubit is then stored until a subsequent zenith opportunity to OGS B, at which point a second  $\theta = 90^\circ$  downlink completes the entangled pair. If  $t_{\text{buffer}}$  is the storage interval between these two zenith opportunities, the memory must satisfy

$$T_{\text{mem}} \geq t_{\text{buffer}}. \quad (29)$$

The effective yield (including memory efficiency  $\eta_{\text{mem}}$ ) is

$$Y_{\text{buff}}(t) = P_{\text{herald}} \eta_{\text{mem}} \eta_A(\theta = 90^\circ, t_{\text{first}}) \times \eta_B(\theta = 90^\circ, t_{\text{second}}), \quad (30)$$

and the corresponding instantaneous SKR is

$$R_{\text{inst,buff}}(t) = \nu(t) \frac{Y_{\text{buff}}(t)}{2} [1 - h(e_X) - f h(e_Z)]. \quad (31)$$

#### D. Memory Efficiency and Multimode Gain

The satellite-borne memory enters the end-to-end yield multiplicatively; for the baseline considered here we use

$$\eta_{\text{mem}} = 0.74 \quad (32)$$

This value is obtained from the analysis shown in Fig. 4 and is obtained by solving the full PDE system for alkali-noble-gas spin exchange and extracting the ratio of retrieved to input quantum-state magnitudes. In addition, the memory supports  $N = 112$  independent temporal modes. For a per-mode success  $P \ll 1$ , the probability of at least one success within a cycle becomes [80]

$$P_N = 1 - (1 - P)^N \approx N P \quad (N = 112), \quad (33)$$

so the buffered downlink geometry benefits from an  $\approx 112\times$  multimode gain in the low-probability regime, compounding the high-elevation link advantage until clocking or readout limits are reached [22, 79].

#### E. Instantaneous SKR

Under the BB84 one-way post-processing bound (Sec. V C), the buffered downlink configuration achieves an instantaneous rate improvement of

$$\mathcal{G} \equiv \frac{R_{\text{inst,buff}}}{R_{\text{inst,dual}}} = 111\times \quad (34)$$

This gain is driven primarily by the reduced zenith slant path (500 km versus 1461.9 km) and persists despite finite  $\eta_{\text{mem}} = 0.74$ . The buffer interval required by the geometry is  $t_{\text{buffer}} = 463$  s, so the operational constraint is  $T_{\text{mem}} \geq 463$  s.

#### F. Scenario Comparison

Table I summarizes the combined per-trial success probability and instantaneous SKR for the two downlink geometries at  $h = 500$  km with an OGS separation of 3267.9 km.

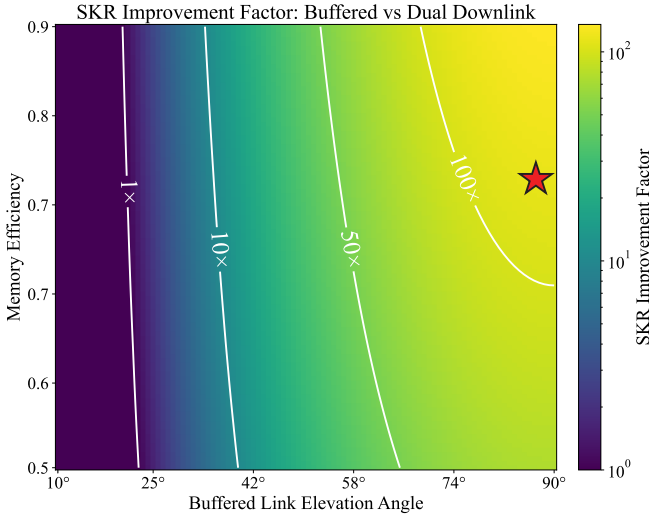


FIG. 6. **SKR improvement for buffered downlink vs. dual downlink.** Heatmap of the instantaneous SKR gain  $\mathcal{G} \equiv R_{\text{inst, buff}}/R_{\text{inst, dual}}$  as a function of buffered-link elevation angle (x-axis) and memory efficiency  $\eta_{\text{mem}}$  (y-axis). Colors (log scale) and iso-contours ( $1\times$ ,  $10\times$ ,  $50\times$ ,  $100\times$ ) show how operating nearer to zenith and improving  $\eta_{\text{mem}}$  increase the advantage of buffering. The red star marks the baseline used in this work ( $\eta_{\text{mem}} \approx 0.74$ ,  $\theta \approx 90^\circ$ ), which yields a  $\gtrsim 10^2\times$  improvement.

TABLE I. Combined per-trial success probability  $\eta$  and instantaneous secret key rate (SKR) at  $h = 500$  km and OGS separation 3267.9 km.

Scenario	Combined $\eta$	SKR (bits/s)
Dual downlink	$4.23 \times 10^{-5}$	$8.12 \times 10^3$
Buffered downlink	$4.70 \times 10^{-3}$	$9.03 \times 10^5$
<b>Improvement factor</b>	<b>111<math>\times</math></b>	<b>111<math>\times</math></b>

For these mission parameters, buffered downlink increases the combined success probability and instantaneous SKR by 111 $\times$ . The required storage interval between zenith contacts is  $t_{\text{buffer}} = 7.7$  min = 463 s; feasibility therefore requires

$$T_{\text{mem}} \geq 463 \text{ s.} \quad (35)$$

## VI. DISCUSSION

### A. Buffered Overhead as an Alternative to Dual Downlink

The results indicate that operating each downlink at zenith with intermediate storage constitutes a compelling alternative method for simultaneous dual downlink. For the baseline geometry ( $h = 500$  km, OGS separation 3267.9 km), the buffered-overhead approach shortens the slant range from 1461.9 to 500.0 km (2.9 $\times$ ) and yields a 111 $\times$  increase in both combined success probability and

instantaneous SKR relative to the 20°/20° case. This improvement arises primarily from reduced diffraction and pointing loss at zenith, which is consistent with the steep  $\eta$ -versus-range/jitter gradients observed in Fig. 5. While the buffered scheme introduces a storage interval between zenith contacts, the required buffer time of  $t_{\text{buffer}} = 463$  s is compatible with the memory parameters considered here.

### B. Near-Term Feasibility of Satellite Quantum Memories

Our calibrated memory efficiency  $\eta_{\text{mem}} = 0.74$  and support for  $N = 112$  temporal modes suggest that meaningful SKR gains are achievable with near-term hardware. In the long-range, low-per-attempt success regime, multimode operation increases the probability of at least one success per cycle approximately linearly with  $N$  [22, 79], which in turn enhances the elevation-angle advantage provided by the buffered geometry. The feasibility condition  $T_{\text{mem}} \geq t_{\text{buffer}} = 463$  s sets a concrete requirement for storage lifetime. The storage decay over this interval is sufficiently small to justify treating  $\eta_{\text{mem}}$  as constant in the SKR evaluation.

From a systems standpoint, the buffered-overhead approach is ideal because it trades stringent pointing at long slant range for a memory-limited duty cycle at short slant range. This reduces sensitivity to microradian-level jitter, which is the dominant penalty in Fig. 5) and shifts engineering effort toward memory stability, control-pulse fidelity, and timing synchronization—all subsystems that can be validated on the ground and subsequently space-qualified.

### C. Payload Integration and Scaling

A practical advantage of this proposal is the physical compactness of the optical cavity. The memory modules considered here have  $\sim 1$  cm dimensions which enables multiple independent memories per satellite without prohibitive mass/volume impact. Such replication supports:

1. *Parallelism*: multiple memories can time-stagger or frequency-division multiplex downlinks to increase effective mode capacity beyond  $N = 112$ .
2. *Redundancy*: cold spares mitigate radiation-induced performance drift and extend mission lifetime.
3. *Functional partitioning*: specialized memories (e.g., longer-storage units dedicated to buffering vs. high-throughput units for bursty operation) allow adaptive scheduling across a pass.

These architectural advantages further strengthen the buffered-overhead strategy and create a path to scaling



SKR without relying solely on aperture growth or ultra-stable pointing.

## VII. CONCLUSION & FUTURE WORK

Our results show that buffered zenith operations can deliver a  $\sim 111\times$  increase in instantaneous SKR relative to simultaneous dual downlink at  $20^\circ$  elevation for the same protocol parameters, which is enabled by shorter zenith slant path (500 km vs. 1462 km) and quantum memory parameters ( $\eta_{\text{mem}} = 0.74$ ,  $N = 112$  temporal modes). The required storage lower bound for this buffer  $t_{\text{buffer}} = 463$  s is compatible with near-term memory performance, motivating buffered overhead as a primary mode for space-to-ground QKD demonstrations.

To build on this work, we outline several research directions that would be interesting to explore:

1. **End-to-end power and mass budget.** Perform a full power budget and thermal analysis to size the spacecraft bus (solar array area, battery capacity, radiator sizing) required to operate all of the required hardware components. A key output of this study would be the estimation of how many memory modules can be hosted per satellite within the mass, volume, and power constraints.
2. **Expanded network simulations.** Extend from single-hop S-G links to multi-repeater constellations, quantifying secret-key throughput for a set experimental time window.
3. **Memory physics and coherence.** Refine device-level models to determine realistic coherence times (including radiation, temperature gradients, wall interactions, and control noise), and assess whether long- $T_{\text{mem}}$  operation can buffer gaps when line-of-sight to an OGS is temporarily unavailable due to cloud cover.

Together, these efforts will help to better inform how the satellite architecture proposed in this study needs to be adapted to support a real-world implementation of this technology.

## VIII. DATA AVAILABILITY

The datasets and code supporting the findings of this study are publicly available in the GitHub repository at the following [link](#). This repository includes all necessary scripts, input data, and results to replicate and build upon the analyses presented in this paper. For questions or potential collaboration opportunities, please reach out to the corresponding author.

## IX. ACKNOWLEDGMENTS

We would like to express our gratitude to Professor Don Towsley, as well as Prateek Mantri and Stav Halder, for their assistance and feedback as we drafted the manuscript and implemented the simulation model.

## X. CONTRIBUTIONS

C.C. initiated and led the project, formulating the research question, designing the simulation methodology, implementing the complete codebase, and drafting most of the manuscript with input from all authors. A.W. assisted in modeling the network, proposed the idea of an instantaneous SKR, and provided extensive feedback on the simulation methodology. C.M. assisted with the literature review and the writing of the manuscript. E.R. assisted in the overall flow of the manuscript, wrote a bulk of the background section, and provided feedback on the proposed satellite design. N.D. assisted in the literature review, as well as the writing of the manuscript.

## XI. COMPETING INTERESTS

The authors declare no competing interests.

- 
- [1] C. M. Knaut, A. Suleymanzade, Y. C. Wei, *et al.*, *Nature* **629**, 573 (2024).
  - [2] M. Aspelmeyer, T. Jennewein, M. Pfennigbauer, W. Leeb, and A. Zeilinger, *IEEE Journal of Selected Topics in Quantum Electronics* (2018), 10.1109/JSTQE.2003.820918.
  - [3] H.-J. Briegel, W. Dür, J. I. Cirac, and P. Zoller, *Physical Review Letters* **81**, 5932 (1998).
  - [4] M. A. Nielsen and I. L. Chuang, *Quantum Computation and Quantum Information: 10th Anniversary Edition* (Cambridge University Press, Cambridge, 2010).
  - [5] R. V. Meter, *Quantum Networking*, 1st ed. (Wiley-ISTE, 2014).
  - [6] V. Martin, J. C. Garcia-Escartin, C. N. Gagatsos, E. Diamanti, P. Walther, A. Leverrier, S. Pirandola, and *et al.*, *EPJ Quantum Technology* **8**, 19 (2021).
  - [7] L. de Forges de Parny, O. Alibert, J. Debaud, and *et al.*, *Communications Physics* **6**, 12 (2023).
  - [8] E. Rotherham, C. Casey, E. F. Rodriguez, K. W. V. Torrez, M. Mashor, and I. Pike, “Advancing free-space optical communication system architecture: Performance analysis of varied optical ground station network configurations,” (2024).

- [9] S. E. Vinay and P. Kok, *Physical Review A* **95**, 052336 (2017).
- [10] A. Sit, F. Bouchard, R. Fickler, J. Gagnon-Bischoff, H. Larocque, K. Heshami, D. Elser, C. Peuntinger, K. Günthner, B. Heim, C. Marquardt, G. Leuchs, R. W. Boyd, and E. Karimi, *Optica* **4**, 1006 (2017).
- [11] S. Pirandola, *Physical Review Research* **3**, 023130 (2021).
- [12] S. Khatri, A. J. Brady, R. A. Desporte, *et al.*, *npj Quantum Information* **7** (2021), 10.1038/s41534-020-00327-5.
- [13] L. de Forges de Parny, O. Alibart, J. Debaud, *et al.*, *Communications Physics* **6**, 12 (2023).
- [14] A. Kalachev, *Bulletin of the Lebedev Physics Institute* **50**, S1312 (2023).
- [15] S. M. Zangi, C. Shukla, A. U. Rahman, and B. Zheng, *Entropy* **25**, 415 (2023).
- [16] A. M. Childs, H. Fu, D. Leung, Z. Li, M. Ozols, and V. Vyas, *arXiv preprint arXiv:2309.16387* (2023), 10.48550/arXiv.2309.16387.
- [17] M. Gündoğan, T. Jennewein, F. K. Asadi, E. D. Ros, E. Sağlamyürek, D. Oblak, T. Vogl, D. Rieländer, J. Sidhu, S. Grandi, L. Mazzarella, J. Wallnöfer, P. Ledingham, L. LeBlanc, M. Mazzera, M. Mohageg, J. Wolters, A. Ling, M. Atatüre, H. de Riedmatten, D. Oi, C. Simon, and M. Krutzik, “Topical white paper: A case for quantum memories in space,” (2021).
- [18] S. J. Yang, X. J. Wang, X. H. Bao, and *et al.*, *Nature Photonics* **10**, 381 (2016).
- [19] C. Liorni, H. Kampermann, and D. Bruß, *New Journal of Physics* **23**, 053021 (2021).
- [20] L. M. Duan, M. Lukin, J. I. Cirac, and P. Zoller, *Nature* **414**, 413 (2001).
- [21] S. H. Wei, B. Jing, X. Y. Zhang, J. W. Liu, K. Y. Liu, Y. Tian, X. J. Liu, J. H. Wu, J. Wu, W. Chen, and X. M. Jin, *npj Quantum Information* **10**, 19 (2024).
- [22] C. Simon, H. de Riedmatten, M. Afzelius, N. Sangouard, H. Zbinden, and N. Gisin, *Physical Review Letters* **98**, 190503 (2007).
- [23] A. Ortu, J. V. Rakonjac, A. Holzäpfel, A. Seri, S. Grandi, M. Mazzera, H. de Riedmatten, and M. Afzelius, *Quantum Science and Technology* **7**, 035024 (2022).
- [24] S. Pirandola, R. Laurenza, C. Ottaviani, and L. Banchi, *Nature Communications* **8**, 15043 (2017).
- [25] S. Pirandola, *Physical Review Research* **3**, 013279 (2021).
- [26] K. Azuma, S. E. Economou, D. Elkouss, P. Hilaire, L. Jiang, H.-K. Lo, and I. Tzitrin, *Reviews of Modern Physics* **95**, 045006 (2023).
- [27] Y. Zheng, H. Sharma, and J. Borregaard, *PRX Quantum* **3**, 040319 (2022).
- [28] S. Abruzzo, H. Kampermann, and D. Bruß, *Physical Review A* **89**, 012301 (2014).
- [29] C. Panayi, M. Razavi, X. Ma, and N. Lütkenhaus, *New Journal of Physics* **16**, 043005 (2014).
- [30] M. Gündoğan, J. S. Sidhu, V. Henderson, *et al.*, *npj Quantum Information* **7**, 128 (2021).
- [31] D. Luong, L. Jiang, J. Kim, and N. Lütkenhaus, *Applied Physics B* **122**, 96 (2016).
- [32] M. J. Bae, N. K. Panigrahy, P. Dhara, M. Z. Hossain, W. O. Krawec, A. Russell, D. Towsley, and B. Wang, “Blockwise post-processing in satellite-based quantum key distribution,” (2025), [arXiv:2503.06031](https://arxiv.org/abs/2503.06031) [quant-ph].
- [33] C. H. Bennett and G. Brassard, *Theoretical Computer Science* **560**, 7 (2014).
- [34] A. K. Ekert, *Physical Review Letters* **67**, 661 (1991).
- [35] A. Mariani *et al.*, in *2023 IEEE International Conference on Quantum Computing and Engineering (QCE)* (Bellevue, WA, USA, 2023) pp. 1389–1393.
- [36] J. W. Fowler, B. R. Shank, W. C. Brown, *et al.*, *PRX Quantum* **5**, 040323 (2024).
- [37] A. Fragner, M. Göppl, J. M. Fink, A. Blais, D. Esteve, and A. Wallraff, *Science* **322**, 1357 (2008).
- [38] W. Xing, Z. Li, *et al.*, “Computing assigned to satellite: Leveraging cots hardware at leo,” (2024), 2401.03435.
- [39] L. You *et al.*, *Optics Express* **26**, 2965 (2018).
- [40] Y.-W. Cho, G. T. Campbell, J. L. Everett, J. Bernu, D. B. Higginsbottom, M. T. Cao, J. Geng, N. P. Robins, P. K. Lam, and B. C. Buchler, *Optica* **3**, 100 (2016).
- [41] Y. O. Dudin, L. Li, and A. Kuzmich, *Physical Review A* **87**, 031801 (2013).
- [42] O. Katz, Y. Peleg, R. Shaham, and O. Firstenberg, *Science Advances* **7**, eabe9164 (2021).
- [43] O. Katz, R. Shaham, and O. Firstenberg, *Physical Review A* **105**, 042606 (2022).
- [44] S. Strangfeld, S. Kanthak, M. Schiemangk, I. Wiegand, A. Wicht, A. Ling, and M. Krutzik, *JOSA B* **38**, 1885 (2021).
- [45] L. Heller, P. Farrera, G. Heinze, and H. de Riedmatten, *Physical Review Letters* **124**, 210504 (2020).
- [46] S.-Y. Lan, A. G. Radnaev, O. A. Collins, D. N. Matsukevich, T. A. B. Kennedy, and A. Kuzmich, *Optics Express* **17**, 13639 (2009).
- [47] Y.-F. Pu, N. Jiang, W. Chang, H.-X. Yang, C. Li, and L.-M. Duan, *Nature Communications* **8**, 15359 (2017).
- [48] M. Langlois, L. De Sarlo, D. Holleville, N. Dimarcq, J.-F. Schaff, and S. Bernon, *Physical Review Applied* **10**, 064007 (2018).
- [49] B. Barrett, L. Antoni-Micollier, L. Chichet, B. Battelier, T. Lévêque, A. Landragin, and P. Bouyer, *Nature Communications* **7**, 13786 (2016).
- [50] H. Müntinga, H. Ahlers, D. Becker, *et al.*, *Physical Review Letters* **110**, 093602 (2013).
- [51] C. Deppner, W. Herr, M. Cornelius, *et al.*, *Physical Review Letters* **127**, 100401 (2021).
- [52] D. Becker, M. D. Lachmann, S. T. Seidel, *et al.*, *Nature* **562**, 391 (2018).
- [53] M. D. Lachmann, H. Ahlers, D. Becker, *et al.*, *Nature Communications* **12**, 1317 (2021).
- [54] L. Liu *et al.*, *Nature Communications* **9**, 2760 (2018).
- [55] D. C. Aveline, J. R. Williams, E. R. Elliott, *et al.*, *Nature* **582**, 193 (2020).
- [56] P. Laurent, D. Massonnet, L. Cacciapuoti, and C. Salomon, *Comptes Rendus Physique* **16**, 540 (2015).
- [57] K. Frye, S. Abend, W. Bartosch, *et al.*, *EPJ Quantum Technology* **8**, 1 (2021).
- [58] D. Devani, S. Maddox, R. Renshaw, *et al.*, *CEAS Space Journal* **12**, 539 (2020).
- [59] Y. A. El-Neaj, C. Alpigiani, S. Amairi-Pyka, *et al.*, *EPJ Quantum Technology* **7**, 6 (2020).
- [60] D. Lago-Rivera, S. Grandi, J. V. Rakonjac, A. Seri, and H. de Riedmatten, *Nature* **594**, 37 (2021).
- [61] X. Liu, J. Hu, Z.-F. Li, X. Li, P.-Y. Li, P.-J. Liang, Z.-Q. Zhou, C.-F. Li, and G.-C. Guo, *Nature* **594**, 41 (2021).
- [62] G. Heinze, C. Hubrich, and T. Halfmann, *Physical Review Letters* **111**, 033601 (2013).

- [63] I. Usmani, C. Clausen, F. Bussi eres, N. Sangouard, M. Afzelius, and N. Gisin, *Nature Photonics* **6**, 234 (2012).
- [64] M. G ndogan, M. Mazzer , P. M. Ledingham, M. Cristian, and H. de Riedmatten, *New Journal of Physics* **15**, 045012 (2013).
- [65] A. Seri, D. Lago-Rivera, A. Lenhard, G. Corrielli, R. Osellame, M. Mazzer , and H. de Riedmatten, *Physical Review Letters* **123**, 080502 (2019).
- [66] N. Sinclair, E. Saglamyurek, H. Mallahzadeh, J. A. Slater, M. George, R. Ricken, M. P. Hedges, D. Oblak, C. Simon, W. Sohler, and W. Tittel, *Physical Review Letters* **113**, 053603 (2014).
- [67] E. Saglamyurek, M. Grima  Puigibert, Q. Zhou, L. Giner, F. Marsili, V. B. Verma, S. W. Nam, L. Oesterling, D. Nippa, D. Oblak, and W. Tittel, *Nature Communications* **7**, 11202 (2016).
- [68] T.-S. Yang, Z.-Q. Zhou, Y.-L. Hua, X. Liu, Z.-F. Li, P.-Y. Li, Y. Ma, C. Liu, P.-J. Liang, X. Li, *et al.*, *Nature Communications* **9**, 3407 (2018).
- [69] E. Saglamyurek, N. Sinclair, J. Jin, J. A. Slater, D. Oblak, F. Bussi eres, M. George, R. Ricken, W. Sohler, and W. Tittel, *Nature* **469**, 512 (2011).
- [70] S. Marzban, J. G. Bartholomew, S. Madden, K. Vu, and M. J. Sellars, *Physical Review Letters* **115**, 013601 (2015).
- [71] G. Corrielli, A. Seri, M. Mazzer , R. Osellame, and H. de Riedmatten, *Physical Review Applied* **5**, 054013 (2016).
- [72] T. Zhong, J. M. Kindem, J. G. Bartholomew, J. Rochman, I. Craiciu, E. Miyazono, M. Bettinelli, E. Cavalli, V. Verma, S. W. Nam, F. Marsili, M. D. Shaw, A. D. Beyer, and A. Faraon, *Science* **357**, 1392 (2017).
- [73] A. M. Dibos, M. Raha, C. M. Phenicie, and J. D. Thompson, *Physical Review Letters* **120**, 243601 (2018).
- [74] P. Jobez, C. Laplane, N. Timoney, N. Gisin, A. Ferrier, P. Goldner, and M. Afzelius, *Physical Review Letters* **114**, 230502 (2015).
- [75] M. G ndogan, P. M. Ledingham, K. Kutluer, M. Mazzer , and H. de Riedmatten, *Physical Review Letters* **114**, 230501 (2015).
- [76] M. Businger *et al.*, *Physical Review Letters* **124**, 053606 (2020).
- [77] M. Afzelius, C. Simon, H. de Riedmatten, and N. Gisin, *Physical Review A* **79**, 052329 (2009).
- [78] S.-H. Wei, B. Jing, X.-Y. Zhang, *et al.*, *npj Quantum Information* **10**, 19 (2024).
- [79] A. Barbosa, H. Ter as, and E. Z. Cruzeiro, arXiv preprint arXiv:2402.17752 (2024), [arXiv:2402.17752](https://arxiv.org/abs/2402.17752).
- [80] J.-W. Ji, F. K. Asadi, K. Heshami, and C. Simon, *Phys. Rev. Appl.* **19**, 054063 (2023).
- [81] A. Ortu, J. V. Rakonjac, A. Holz pfel, A. Seri, S. Grandi, M. Mazzer , H. de Riedmatten, and M. Afzelius, *Quantum Science and Technology* **7**, 035024 (2022).
- [82] M. Dassi , G. Giorgi, P. N. Dominguez, L. Bl mel, and C. Gohle, in *Proceedings of the 36th International Technical Meeting of the Satellite Division of The Institute of Navigation (ION GNSS+ 2023)* (The Institute of Navigation, Denver, Colorado, 2023) pp. 3190–3204.
- [83] N. Ahmadi, S. Schwertfeger, P. Werner, L. Wiese, J. Lester, E. Da Ros, J. Krause, S. Ritter, M. Abasifard, C. Cholsuk, R. G. Kr mer, S. Atzeni, M. G ndogan, S. Sachidananda, D. Pardo, S. Nolte, A. Lohrmann, A. Ling, J. Bartholom us, G. Corrielli, M. Krutzik, and T. Vogl, *Advanced Quantum Technologies* **7**, 2300343 (2024).
- [84] R. Bedington, J. M. Arrazola, and A. Ling, *npj Quantum Information* **3**, 30 (2017).
- [85] D. Beysens, *Frontiers in Space Technologies* **3**, 1092802 (2022).
- [86] C. E. Niederhaus and F. J. Miller, *Intravenous Fluid Mixing in Normal Gravity, Partial Gravity, and Microgravity: Down-Selection of Mixing Methods*, NASA Technical Memorandum NASA/TM-2008-215000 (NASA Glenn Research Center, Cleveland, Ohio, 2008).
- [87] S. Selvadurai, A. Chandran, D. Valentini, and B. Lamprecht, *Applied Sciences* **12**, 2858 (2022).
- [88] Q. Zhang, F. Xu, Y.-A. Chen, C.-Z. Peng, and J.-W. Pan, *Optics Express* **26**, 24260 (2018).
- [89] E. R. Elliott, M. C. Krutzik, J. R. Williams, *et al.*, *npj Microgravity* **4**, 16 (2018).
- [90] D. Binder, E. C. Smith, and A. B. Holman, *IEEE Transactions on Nuclear Science* **22**, 2675 (1975).
- [91] H. Daneshvar, K. G. Milan, A. Sadr, M. Ghasemi, and S. Abrishami, *Scientific Reports* **11**, 20657 (2021).
- [92] L. Ma, M. A. Viray, D. A. Anderson, and G. Raithel, *Phys. Rev. Appl.* **18**, 024001 (2022).
- [93] NASA Small Spacecraft Systems Virtual Institute (S3VI), *State-of-the-Art of Small Spacecraft Technology: Chapter 7 — Thermal Control (2024 Edition)*, Technical Report (National Aeronautics and Space Administration, Moffett Field, CA, USA, 2025).
- [94] O. Katz, R. Shaham, and O. Firstenberg, *PRX Quantum* **3**, 010305 (2022).
- [95] R. Shaham, O. Katz, and O. Firstenberg, *Nature Physics* **18**, 506 (2022).
- [96] Y. Gensterblum, A. Ghanizadeh, R. J. Cuss, A. Amann-Hildenbrand, B. M. Krooss, C. R. Clarkson, J. F. Harrington, and M. D. Zoback, *Journal of Unconventional Oil and Gas Resources* **12**, 87 (2015).
- [97] X. Wang, M. Ye, F. Lu, Y. Mao, H. Tian, and J. Li, *Biosensors* **12**, 165 (2022).
- [98] Y. Chang and J. Qin, *Physical Review A* **109**, 023113 (2024).
- [99] Z. Wu, *Reviews of Modern Physics* **93**, 035006 (2021).
- [100] T. R. Gentile, P. J. Nacher, B. Saam, and T. G. Walker, *Reviews of Modern Physics* **89**, 045004 (2017).
- [101] X. Ma, C.-H. F. Fung, and H.-K. Lo, *Physical Review A* **76**, 012307 (2007).
- [102] R. Tr nyi and N. L tkenhaus, *Physical Review A* **101**, 012325 (2020).
- [103] J. Walln fer, F. Hahn, M. G ndogan, *et al.*, *Communications Physics* **5**, 169 (2022).

## Appendix A: Probability of establishing a link

We model each elementary connection as four statistically independent processes, following the Supplementary Information in Ref. [103]. See the full derivation in the cited references, but the main points are summarized below.

1. **Memory Efficiency**  $\eta_{\text{mem}}$ . Probability to convert an incoming photon into a stationary qubit and retrieve it later. From the results of this study, we adopt  $\eta_{\text{mem}} = 0.74$ .
2. **Detector Efficiency**  $\eta_{\text{det}}$ . Single-photon detection at the readout terminal. Given demonstrated SNSPD performance, we adopt  $\eta_{\text{det}} = 0.7$  for ground stations which is consistent with [103].
3. **Atmospheric Transmission**  $\eta_{\text{atm}}(\theta)$ . Beer-Lambert scaling with elevation angle  $\theta$ :  

$$\eta_{\text{atm}}(\theta) = (\eta_{\text{atm}}^z)^{1/\sin\theta}, \quad \eta_{\text{atm}}^z = 0.8 \quad (\lambda \approx 795 \text{ nm}), \quad (\text{A1})$$

appropriate for clear-sky mid-latitude conditions [12, 30].
4. **Diffraction and Pointing Loss**  $\eta_{\text{dif}}(l)$ . Beam spreading and residual pointing jitter over slant range  $l$ . A paraxial, diffraction-limited Gaussian emitted with waist  $w_0$  obeys

$$I(r, 0) = I_0 e^{-2r^2/w_0^2}, \quad (\text{A2})$$

$$\theta_d = \frac{\lambda}{\pi w_0}, \quad (\text{A3})$$

$$w(z) = w_0 \sqrt{1 + \left(\frac{\theta_d}{w_0} z\right)^2}, \quad (\text{A4})$$

$$I(r, z) = I_0 \left(\frac{w_0}{w(z)}\right)^2 e^{-2r^2/w(z)^2}. \quad (\text{A5})$$

Pointing jitter is modeled as a 2D Gaussian with standard deviation  $\sigma_p$ :

$$g_p(\mathbf{r}) = \frac{1}{2\pi\sigma_p^2} \exp\left(-\frac{\|\mathbf{r}\|^2}{2\sigma_p^2}\right). \quad (\text{A6})$$

The far-field intensity is the 2D convolution (compact two-column form):

$$\begin{aligned} \tilde{I}(\mathbf{r}, z) &= \int_{\mathbb{R}^2} d^2\boldsymbol{\rho} I(\boldsymbol{\rho}, z) g_p(\mathbf{r} - \boldsymbol{\rho}) \\ &= (I * g_p)(\mathbf{r}; z). \end{aligned} \quad (\text{A7})$$

Collected power through a circular aperture of radius  $R_{\text{rec}}$  at range  $l$  is

$$P(l) = \int_0^{R_{\text{rec}}} \rho d\rho \int_0^{2\pi} d\varphi \tilde{I}(\rho, l), \quad (\text{A8})$$

$$\eta_{\text{dif}}(l) = \frac{P(l)}{P_0}. \quad (\text{A9})$$

For well-stabilized platforms with  $\sigma_p \lesssim 3 \mu\text{rad}$ , receiver-side mispointing is typically negligible because the telescope field of view  $\gg \theta_d, \sigma_p$ .

**Single-shot success probability.** The overall probability for an elementary link is thus

$$\eta = \eta_{\text{mem}} \eta_{\text{det}} \eta_{\text{atm}}(\theta) \eta_{\text{dif}}(l). \quad (\text{A10})$$

### 1. Geometric Dependence

Elevation  $\theta$  and slant range  $l$  from ground-track separation  $L_g$  and satellite altitude  $h$ :

$$l^2 = R_E^2 + (R_E + h)^2 - 2R_E(R_E + h) \cos\left(\frac{L_g}{R_E}\right), \quad (\text{A11})$$

$$\theta = \frac{\pi}{2} - \frac{L_g}{R_E} - \arcsin\left[\frac{R_E}{l} \sin\left(\frac{L_g}{R_E}\right)\right], \quad (\text{A12})$$

with  $R_E = 6,371 \text{ km}$ .

## Appendix B: Simulation-Parameter Tables

TABLE II. Communication-Link Parameters.

Parameter	Value
Operating wavelength $\lambda$	795 nm
Receive aperture $D_r$	1.0 m
Beam-divergence half-angle $\theta_d$	3 $\mu\text{rad}$
Pointing-jitter rms $\theta_{\text{err}}$	1 $\mu\text{rad}$
Minimum elevation angle	20°

TABLE III. Quantum Satellite Parameters.

Parameter	Value
Source repetition rate $R_{\text{rep}}$	90 MHz
Memory efficiency $\eta_{\text{mem}}$	0.74
Detector efficiency $\eta_{\text{det}}$	0.70
Bell-state-measurement efficiency	0.50
Memory modes	112
Entangled-photon source efficiency	0.20
QND-measurement efficiency	0.80

TABLE IV. Orbital Parameters.

Parameter	Value
Earth radius $R_E$	6,371 km
Satellite altitude $h$	500 km



TABLE V. Atmospheric Parameters.

Parameter	Value
Ground turbulence $C_n^2$	$1.7 \times 10^{-14} \text{ m}^{-2/3}$
Turbulence scale height	1 500 m
Relative humidity	0.60

TABLE VI. Fundamental Constants.

Constant	Value
Speed of light $c$	$3.0 \times 10^5 \text{ km s}^{-1}$
Planck constant $h$	$6.62607015 \times 10^{-34} \text{ J s}$